2024 IEEE International Conference on Robotics and Automation (ICRA 2024)
May 13-17, 2024. Yokohama, Japan

Design and validation of slender extensible continuum robot for solar wing re-unfolding in aerospace

Pengyuan Wang, Zheng Zheng, Jiazhen Sun, Yuqiang Liu, Zongbo He, Zhiguang Xing, *Member, IEEE,* Jianwen Zhao, *Member, IEEE*

***Abstract*— The solar array wing deployment of orbiting satellites cannot be performed due to power failure of the connector caused by uncertain loads such as high temperature or vibration in the launching process of the spacecraft. There is currently a lack of suitable unlocking solutions for solar wing re-unfolding. This paper proposes a solution in which an extensible continuum robot (ECR) carrying the unlocking device enters the gap between the satellite and the solar wing, re-unlocking the solar wing. This solution effectively leverages the advantages of ECR collision buffering and adaptable maneuverability within confined space. In response to the proposed solution, the designed ECR with two segments helical spring structure features scalability, hollowness, lightweight, and a big length-diameter ratio. To perform the critical unlocking task, an end effector with the function of loosening and unplugging the aerospace connector for communication is designed based on the drive device away from itself to reduce the inertia of the manipulator. The information from the cameras and force sensors is used to estimate the extent of task execution. We establish an experimental setup to simulate the process of unlocking. The results validate that the ECR successfully accesses the gap (65mm) and accomplishes the unlocking task. The ECR has great application potential for on-orbit service.**

I. Introduction

Continuum robots are composed of a deformable elastic skeleton [1], usually driven by tendons or soft pneumatic actuators to generate bending deformation [2]. Due to its slender and flexible features, it has become the focus of applications in narrow and non-structural environments [3], such as minimally invasive surgery [4, 5], aeroengine maintenance [6, 7], explosive ordnance disposal [8], flexible grasp [1, 10], etc. In the on-orbit service fields, rigid robotic arms have been used to perform repairing satellites [11]. Recently, some researchers have tried to study the dynamic model [12, 13] and motion planning [14] of tendon-driven rigid link manipulators for satellite repair, while there are currently very few feasible solution validations for specific task execution.

The failed deployment of the solar wings [15] is one of the most terrible malfunctions of artificial earth satellites. For a few special critical satellites, this will cause huge economic losses [16]. The remedial action for the inoperative release mechanism [17]-[20] is to re-power it with a device to achieve the goal of unfolding the solar panel. This article innovatively proposes a detailed repair plan, as shown in Fig.1: (1) Send maintenance satellite carrying equipment to approach and mate with the faulty satellite. The continuum robot spirals in the body of the maintenance satellite like a snake; (2) The robot stretches out from the main body of the maintenance satellite, bends 90°, and accesses the 65 mm gap between the satellite and the solar wing; (3) The end effector reaches the operational position and accomplishes the unlocking task which includes heating, loosening, unplugging, and re-power the aerospace connector. By analyzing space requirements, the technical indexes of the proposed ECR can be specified as follows: (i) arm length no less than 1200 mm for entering the specified maintenance position; (ii) arm diameter no more than 50 mm in order to enter into the gap; (iii) payload of 250 g at the tip to ensure that the required end-effectors can be applied; (iv) torque output of 0.9 N·m from end-effector to loosen the aerospace connector.

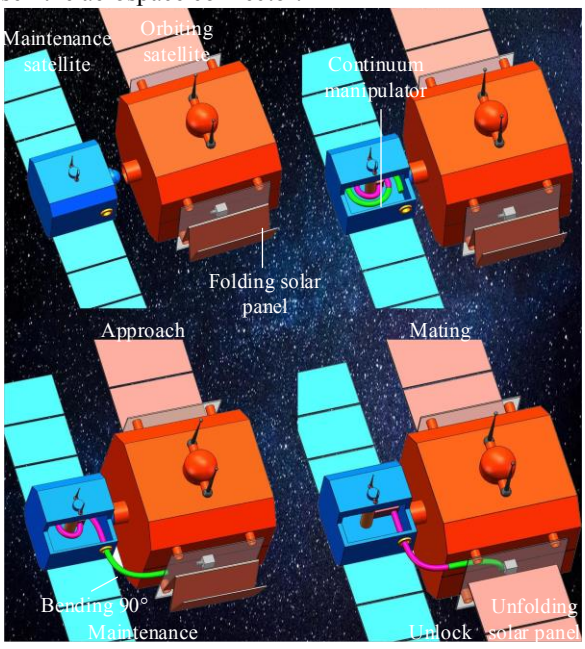

Fig. 1. Repair the solution to re-unlock the solar wing.

For scenarios characterized by confined spatial conditions and the presence of obstacles [15], a bigger length-to-diameter

This work was supported in part by the Yangtze River Delta HIT robot technology research institute under Grant No. HIT-CXY-IEP-SRIMC-21-01, in part by the National Natural Science Foundation of China under Grant No. 52205010, in part by the China Academy of Space Technology under CAST-2021-01-03. *(Correspond author: Zhiguang Xing.)*

Pengyuan Wang, Jiazhen Sun, Zhiguang Xing, and Jianwen Zhao are with Mechanical Engineering, Harbin Institute of Technology, Weihai 264209, China (e-mail: wangpengyuan329@163.com; 15666309919@163.com; zhiguangx_hit@163.com; zhaojianwen@hit.edu.cn). Pengyuan Wang, Zhiguang Xing, and Jianwen Zhao are with Yangtze River Delta HIT Robot Technology Research Institute, Wuhu 241000, China. Zheng Zheng is with this institution too (e-mail: wuhuzhengzheng @126.com).

Yuqiang Liu, and Zongbo He are with the Beijing Institute of Spacecraft System Engineering, Beijing 100081, China (e-mail: echo33151223 @sina.com; 13810528603@139.com).

ratio ECR (meeting technical requirements) emerges as the optimal choice for effectively executing maintenance tasks. According to driven mechanisms, the existing big length-to-diameter ratio continuum robot can generally be categorized into two types: pneumatic and tendon-driven. Festo's BionicMotionRobot [21], inspired by an elephant's trunk, has 12 degrees of freedom and features a length of 800 mm and diameter of 100 mm as a typical representative of a lightweight pneumatic robot, with its flexible bellows structure enabling powerful, dynamic and safe collaborative motions. Jiang [22] introduced a honeycomb pneumatic network architecture characterized by high flexibility and substantial load-bearing capacity. Through a hierarchical control approach, this framework addresses manipulation challenges encountered in scenarios of uncertainty. However, the majority of pneumatic robotic arms [23, 24] have diameters exceeding 50 mm, which imposes limitations on confined and unstructured environments. Tendon-driven continuum robotics have the potential to simultaneously fulfill requirements for both size and rigidity. Dong [25] proposes an extra slender continuum robot which is a hybrid mechanism composed of a combination of compliant and rigid joints capable of supporting a payload 136.2 g. Kang [26] devised a mechanism for enhancing stiffness variation of over 287% using shape memory alloy springs on a continuum robot with a length of 900 mm. Furthermore, rigid link hyper-redundant robots [12]-[14] possess the capability to handle high loads over significant lengths. However, it exhibits limited flexibility due to joint angle limitations or constraints. Rigid collisions are more likely to damage the structure of the solar wing. Designing an ECR to meet the aforementioned technical requirements and enable the re-unfolding of solar array panels is an urgently pressing challenge. Currently, existing continuum robots cannot fulfill this function.

In this paper, we aim to design a two-segment ECR featuring a big length-to-diameter ratio, characterized by its omnidirectional pose-adjusting capabilities. Notably, its terminal section is engineered to accommodate both a camera and the essential actuation components required for the solar panel unlocking simulation processes. Section II introduces the structural design of continuum robots, which fulfill design requisites characterized by small diameter, extensive length, and high load-bearing capacity. The paramount focus lies in crafting an end effector that possesses the capability to loosen and unplug aerospace connectors through a clamping mechanism. Additionally, it encompasses the functionality to melt thread-locking adhesive using heat and repower the connector. The structure parameters of the continuum robotic arm are determined through a combined approach of optimization and finite element simulation. In section III, the designed continuum robotic system is manufactured and subsequently subjected to experimental validation using the constructed test platform. The conclusion and the future work are discussed in section IV.

II. Design of The Extensible Continuum Robot

A. Robotics system design

The designed robotic system, as illustrated in Fig. 1, predominantly comprises a drive system, a two-segmented continuum robotic manipulator, and an end effector.

The drive system (Fig. 2 (a)) consists of six sets of winding devices, each comprising components such as a stepping motor, guide wheel, winding roller, leading screw, and scroll wheel. The guide wheel of each winding device is positioned at varying heights, functioning as fixed pulleys that alter the direction of the driving thread, aligning it with the six holes on the output cover plate. Around the winding wheel, there are four scroll wheels purposefully placed to maintain optimal tension on the driving thread, preventing any occurrence of slackness or entwining within the grooves. The leading screw and the winding roller are threaded in conjunction, with both possessing identical screw pitch values. As the winding roller advances along the lead screw by one pitch, the tendon also progresses through the winding roller by an equivalent pitch. This arrangement ensures that the tendon remains consistently positioned around the guide wheel during the working process.

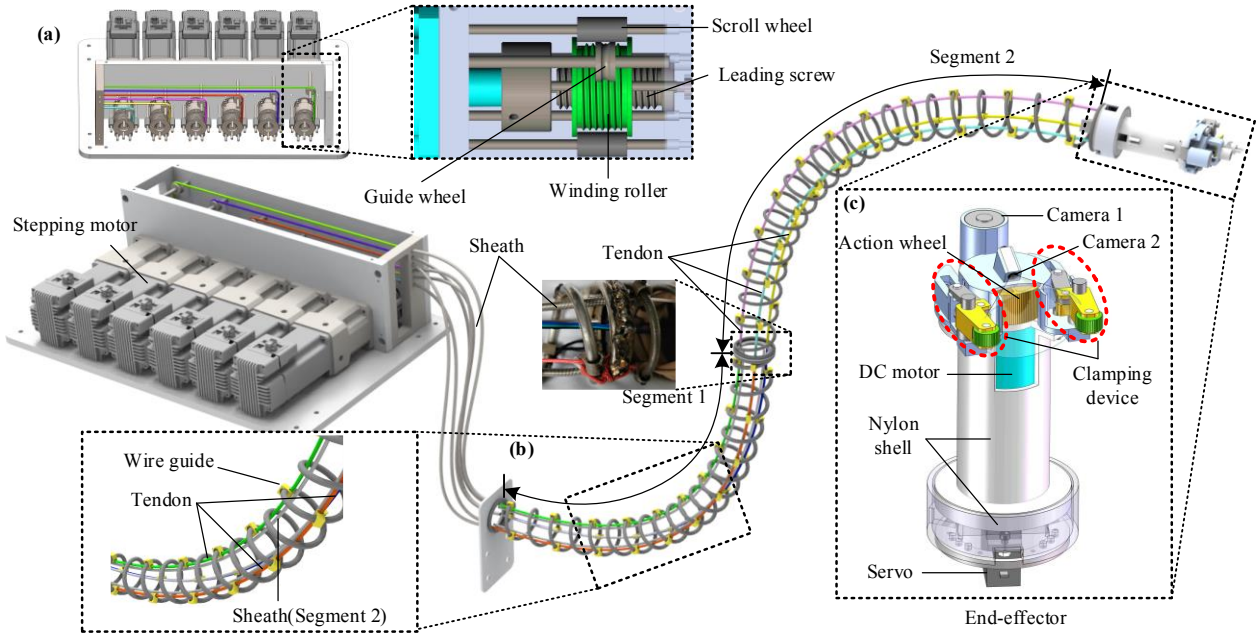

Fig. 2. Design of the proposed continuum robotic system: (a) Drive system; (b) The continuum manipulator; (c) The end effector.

The continuum robotic manipulator is fabricated through the welding assembly of two segments composed of steel springs with different wire diameters and the effective coil count. Each segment of the robotic arm is controlled by three tendons that pass through the wire guide distributed at 120-degree intervals around the circumference (Fig. 2 (b)). Employing hollow tightly coiled springs as tendon sheaths, one end is securely affixed to the output aperture of the drive system, while the opposite end is anchored to the proximal extremity of each robotic arm segment. The sheath of the tendon for the second robotic arm segment passes through the hollow cavity of the first segment. When a tendon is pulled, the manipulator bends in the direction of this rope. The length of the manipulator becomes shorter when the three tendons are pulled simultaneously.

B. End-effector Design

The structure of the end effector is composed of elements including a clamping mechanism, a DC motor, an action wheel, two cameras, a servo motor, and a high-performance nylon housing, as shown in Fig. 2 (c). The servo motor enables the end effector to rotate around its central axis, thereby facilitating the clamping mechanism to securely grip aerospace connectors from different orientations. The camera device includes a front-facing camera (Camera 1) and a lateral camera (Camera 2). The front-facing camera has a diameter of 12 mm and 5 million pixels, providing real-time feedback of the directly ahead view. On the other hand, the lateral camera has a diameter of 3.5 mm and 1 million pixels, mainly used to observe the distance and gripping orientation between the clamping mechanism and the aerospace connector. The DC gear-reduced motor (Shenzhen Mingyang Motor's JGA25-370 model) is chosen to ensure output torque.

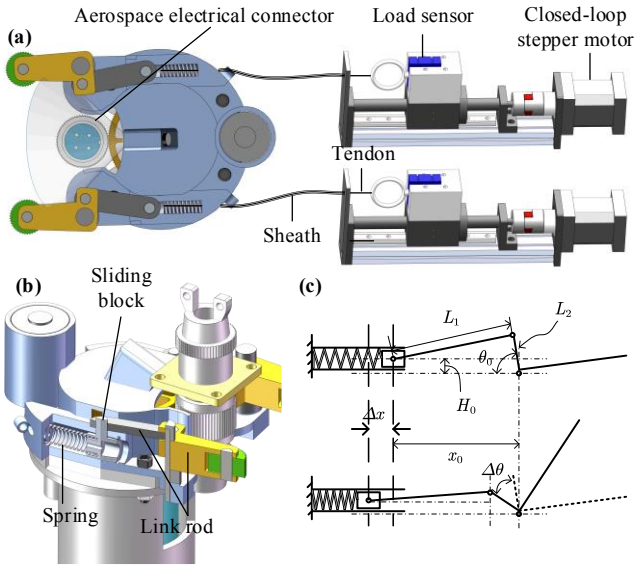

Fig. 3. The design and principle of the clamping mechanism: (a) The driving mode of the clamping device; (b) A three-dimensional sectional view of the clamping mechanism; (c) A schematic representation depicting the operational principle of the clamping mechanism.

The clamping mechanism in Fig. 3 is designed based on the tendon-driven principle. The linear displacement platform (Fig. 3 (a)) is positioned behind the ECR, which results in reduced weight and offers substantial power output. The sliding platform pulls the tendon backward, causing the slider to compress the spring and initiate the linkage. As a result, the handle rotates around a fixed axis, achieving the function of clamping the aerospace connector. Conversely, under the restorative force of the spring, the handle undergoes a reverse rotation, completing the action of releasing the connector. In the tightened state of the clamping mechanism, the action wheel torqued by the DC motor results in the loosening of the nut on the aerospace connector. The external tooth profile of the action wheel is specifically designed according to the straight-threaded screw thread structure of the nut, aiming to enhance the contact area and increase friction.

The stiffness of the spring within the clamping mechanism is a crucial parameter in achieving the rebound of the gripper. From the three-dimensional model (Fig. 3 (b)), the parameters in the initial state can be obtained. In Fig. 3 (c), L_1 and L_2 are the lengths of the handle and connecting rod, respectively. x_0 denotes the lateral distance from the block to the handle's pivot axis, while H_0 signifies the vertical distance. θ_0 stands for the angle between the handle's short arm and the direction of slider movement. Utilizing the Pythagorean theorem, the relationship between Δx and $\Delta\theta$ can be determined:

$$\begin{aligned}(L_2\sin(\theta_0-\Delta\theta)-H_0)^2+(x_0+\Delta x-L_2\sin(\theta_0-\Delta\theta))^2\\=L_2\end{aligned} \tag{1}$$

Assuming the initial length of the spring is 25 mm. When placed within the clamping mechanism, it becomes compressed to a length of 13.8 mm. The initial compression amount can be calculated as Δx_0=11.2 mm. The spring force can be deduced as follows:

$$\begin{aligned}F=k\Big(\sqrt{L_2-(L_2\sin(\theta_0-\Delta\theta)-H_0)^2}-x_0+\\L_2\sin(\theta_0-\Delta\theta)+\Delta x_0\Big)\end{aligned} \tag{2}$$

It is evident that the angle $\Delta\theta$ equals 46° when the clamping mechanism is in the state of gripping the connector. At this point, the spring's restoring force is harnessed to counteract the cumulative friction forces, encompassing the resistances between the slider and the nylon casing, as well as the tendon and its sheath, among others. By setting the friction force to 16 N, the spring stiffness k can be calculated by equation (2) as 1.38 N/mm. Hence, it is reasonable to choose a spring characterized by a medium diameter of 4.4 mm, a spring wire diameter of 0.6 mm, and an effective number of turns amounting to 11.

C. Determination of Structure Parameters for ECR

It is a challenge to determine reasonable structure parameters for guaranteeing the end load capacity of the robot. According to the technical requirements, we determined that a single segment length is H = 600 mm and an outer diameter is Φ = 50 mm. The optimization parameters include the wire diameter d and the effective coil number n.

To determine the structure parameters, we have adopted the method of combining conditional constraint and finite element simulation. Firstly, according to the spring manual [27], the formulas which include the deformation of the spring under radial load, the spring mass, and the shear stress when the spring is compressed are obtained. Subsequently, we derive the spring parameters through the constraints imposed.

Finally, the spring's three-dimensional model established element software. A finite element model depicting the deformation of the tendon-driven spring under external forces has been constructed. If simulation results indicate that the tendon-driven arm can perform the lifting motion under end-effector load, then the spring parameters are considered valid. Otherwise, we should adjust the constraints and recalculate the parameters. Taking the second segment of a continuum manipulator as an example, the structural parameters are determined.

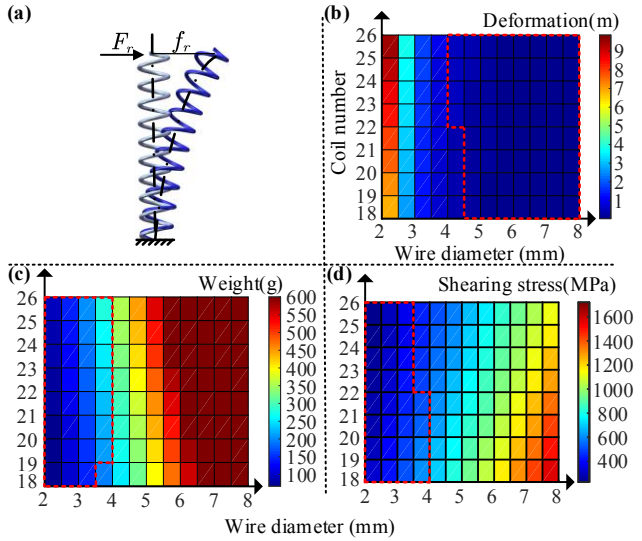

Fig. 4. Performance under different spring parameters: (a) Deformation diagram from the radial load; (b) Radial deformation; (c) Spring mass; (d) Shearing stress.

The deformation of the spring under radial load is shown in Fig. 4 (a). The formula for calculating the lateral deformation is as follows:

$$f_r = \frac{8F_r n D^3}{E d^4}\left[1+\frac{4}{3}\left(\frac{H}{D}\right)^2(2+\mu)\right] \tag{3}$$

Where D is the middle diameter of the spring. E and μ are the elastic modulus and Poisson's ratio of the material respectively. The radial load $F_r = 3$ N is obtained by multiplying the weight of the end effector by a safety factor of 1.2. According to the conclusions from [28], the tip displacement of a tendon-driven continuum robotic arm is four times greater than that of a non-tendon-driven one under radial load. In this case, the constraint condition is set as $f_r < 0.5$ m. The structure parameters that satisfy the conditions are depicted within the red area in Fig. 4 (b). Then, the spring-mass is calculated as follows:

$$M = 1.937\times10^{-5} D d^2 n \tag{4}$$

Considering the actual situation that the first segment of the arm bears the weight of both the second segment and the end effector, it is imperative to minimize the weight of the second segment. A mass constraint is $M < 350$ g with the red area as shown in Fig. 4 (c). The final constraint is the shear stress. The formula for calculating the deformation and shear stress of the spring under axial load F is based on the obtained parameters is imported into finite

$$f = \frac{8FC^3 n}{Gd}$$
$$\tau = \frac{8FC}{\pi d^2} \tag{5}$$

Where G is the shear modulus of the material and $C=D/d$. Ultimate shear stress is $\tau < 0.45\sigma_b = 607.5\text{MPa}$. σ_b is the tensile strength of the material.

Setting the compressive deformation as $f = 300$ mm, Fig. 4 (d) shows that parameters in the red area satisfy the condition. Based on the three specified constraints, the parameters for the second segment can be determined as $d = 4$ mm and $n = 22$ by finding the intersection of the red region.

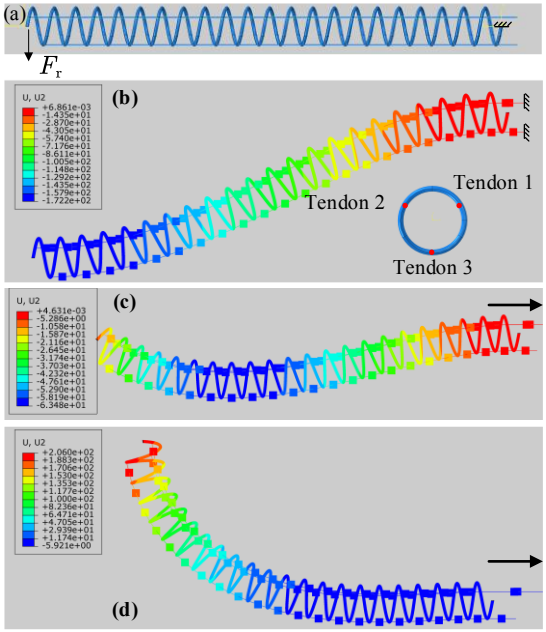

Fig. 5. Finite element simulation of tendon-drive spring: (a) Finite element model; (b) Spring displacement cloud image with the tendon unstretched; (c) and (d) correspond to the tendon 1 and 2 being pulled.

The simulation model shown in Fig. 5 (a) is built. We utilize a slip ring connection type to simulate the tendon--drive. Under the condition where the proximal tendon is fixed, the displacement contour of the spring under load is illustrated in Fig. 5 (b). The maximum displacement of 172.2 mm at the tip of the arm signifies a noticeable increase in the stiffness of the spring due to the implementation of the tendon-driven mechanism. When traction is applied to tendons 1 and 2, the spring's tip returns to the horizontal position (Fig. 5 (c)). The spring can lift the end load by increasing the traction of tendons 1 and 2, as shown in Fig. 5 (d). In conclusion, the chosen spring parameters can meet the requirements. The parameters of the two-segment ECR are listed in Table I.

Table I: Structural parameters of a continuum manipulator

Number	Φ (mm)	H(mm)	d (mm)	n
Segment 1	50	600	5	17
Segment 2	50	600	4	22

III. Experimental Validation

In order to simulate the unlocking experiment of the ECR, a testing platform system is established in Fig. 6. This system encompasses the capability to control the robotic arm in both vertical and horizontal directions. The ECR is fixed to the platform system. Each segment possesses three degrees of freedom, whereas the end-effector has four. In addition, we have utilized two acrylic panels to create a simulated body with a 65 mm gap.

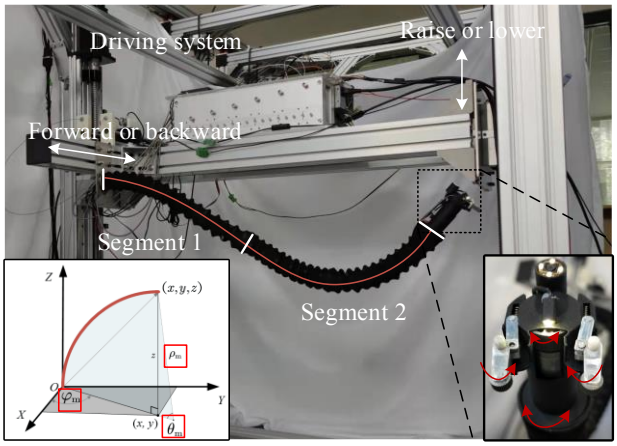

Fig. 6. Test platform.

A. Simulated unlocking process

The simulation process of loosening and unplugging the aerospace connector can be found in Supplementary Video 1. The initial state of the continuum robotic arm is illustrated in Fig. 7 (a). The operator uses a handle to control the 90-degree bending direction of the segment 1, aligning the end effector with the narrow gap of the simulated body, as shown in Fig. 7 (b). Secondly, the platform system is utilized to control the soft manipulator arm access into the narrow gap. The end effector reaches the operational position of the aerospace connector (Fig. 7 (c)) by adjusting the pose of the manipulator. Third, the end effector's clamping mechanism is released, and the second segment of ECR is adjusted to position the connector within the gripping mechanism's operational range. The clamping mechanism is tightened to securely hold the connector (Fig. 7 (d)). Subsequently, with the end effector constrained, the angle of the end effector is adjusted to align it parallel to the connector (Fig. 7 (e)). Afterwards, the DC motor within the end effector drives the action wheel to rotate slowly (12 revolutions per minute) to make the nut loosened (Fig. 7 (f)). The extent of nut loosening can be observed through the camera 2 mounted on the end-effector. Finally, the clamping mechanism is released, and the end effector is slightly moved forward before re-tightening the clamping mechanism. This action causes the auxiliary wheel in the hand to engage the front end of the nut. As the ECR moves backward, the connector is unplugged.

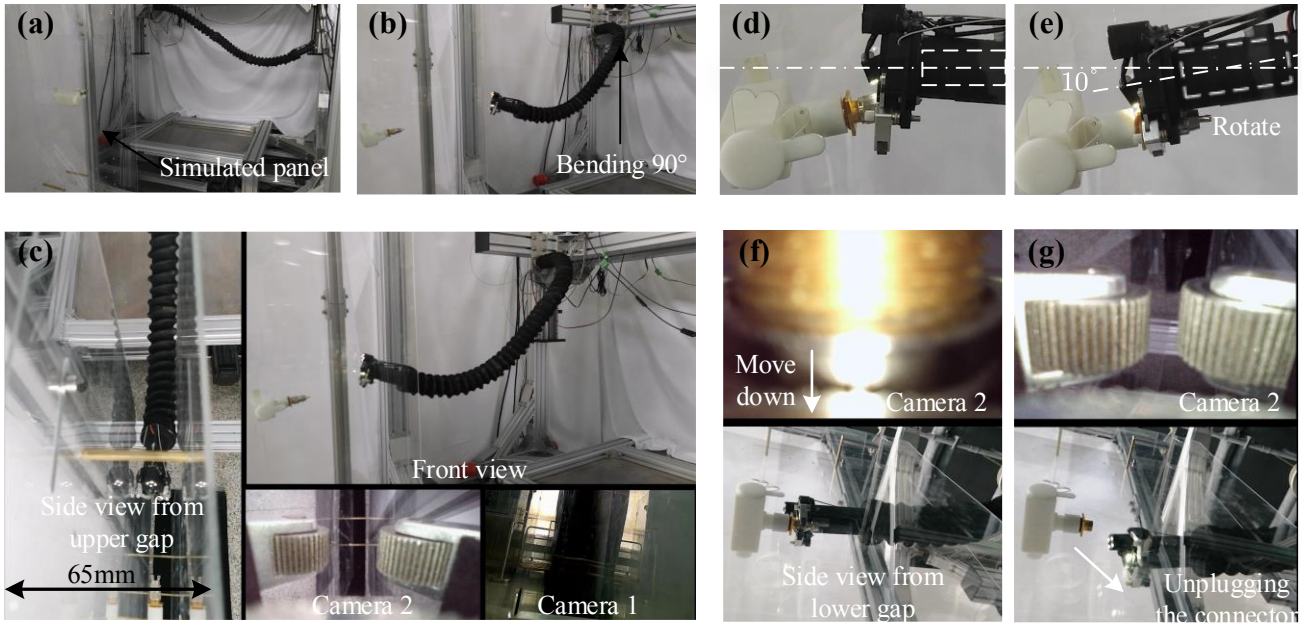

Fig. 7. The proposed ECR achieves the function of loosening and unplugging aerospace connectors. (a) Initial state; (b) Bending 90°; (c) Accessing gap; (d) Approaching the connector; (e) Holding the connector; (f) Loosening the nut; (g) unplugging the connector.

B. Driving force experiment of clamping mechanism

The variation of force sensors (Fig. 3 (a), Supplementary Video 2) during the aerospace connector clamped, loosened and unplugged process is shown in Fig. 8. State 1 with a traction force of 50 N cannot loosen the nut by the active wheel. With the traction force increased to around 70 N, the gripping mechanism holds the connector even more securely, and at this point, the nut is gradually loosened. Upon reaching State 2, it's observed that the connector nut has moved a certain distance backward. If the active wheel continues to be driven, it could result in a reduced contact area between the action wheel and the nut. This reduction in contact area might hinder the transmission of torque. Hence, the clamping mechanism is momentarily relaxed, and a slight backward movement of the end-effector is executed. After re-gripping the nut, the active wheel is driven. In State 3, it is indicated that the nut has been completely loosened. To ensure the reliability of extracting the connector plug, we adopt the

strategy of State 4, as shown in the lateral view of Fig. 8. By utilizing the manipulator to move the end-effector backward,

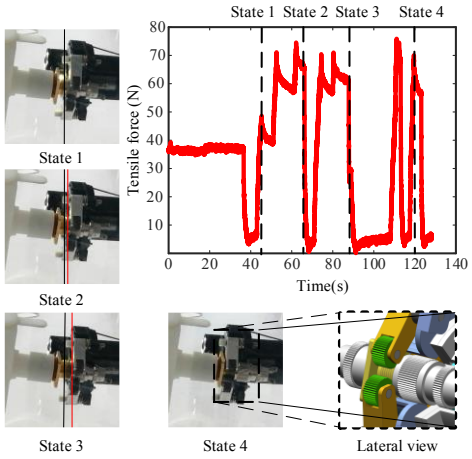

Fig. 8. Assessing the level of clamping based on the tension force values.

the connector can be pulled out effectively. Based on the conducted experiments, it can be concluded that utilizing force sensors for feedback enables the perception of the clamping extent of the gripping mechanism.

C. *Heating test.*

The aerospace connector's nut and threads might be secured with thread adhesive for a firm connection. It's necessary to use a heating method [29,30] to soften the adhesive so as to facilitate the disassembly of the aerospace connector. In Fig. 9 (a), we have hollowed out the middle section of the clamping device's handle and wound it with nichrome alloy resistance wire (a diameter of 0.4 mm). The heat is transferred to the nut by means of heating the handle.

In the experiment, the adjustable DC-regulated power supply outputs a current of 4A. The surface temperature of the clamping mechanism and the connector observed by the thermal imager is shown in Fig. 9 (b). The experimental procedure demonstrates that the surface of the aerospace connector can be heated to 100°C to creating conditions conducive to the melting of the thread adhesive.

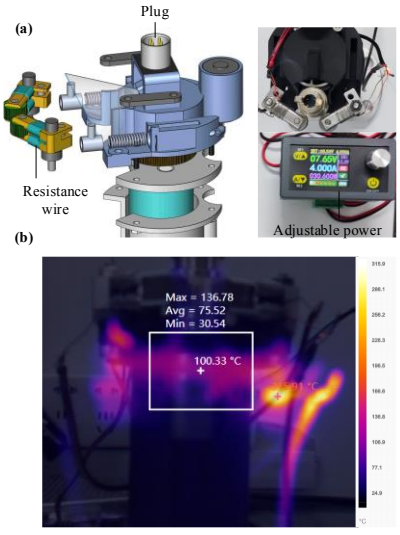

Fig. 9. Heating test. (a) Nickel-chromium resistance wire heating method. (b) The surface temperature is measured using a thermal imager.

IV. Conclusion

This paper proposes a solution involving the use of an ECR to address the issue of unopened solar wings on satellites. We have designed a two-segment helical structure for a continuum robotic system, endowing its end-effector with the ability to loosen and unplug aerospace connectors. We employ a combined approach of constraint optimization and finite element simulation to determine the structure parameters of the spring. The actual mass of the manipulator is only 810g. Moreover, a clamping device has been devised, capable of performing designated tasks with the assistance of a camera and load sensor. The stiffness of the return spring can be calculated by analyzing the working principle of the clamping mechanism. Through experiments, the ECR has been validated to meet design requirements. It successfully accomplished tasks including lifting the end effector, bending the first segment by 90 degrees, entering a 65 mm gap with the second segment, and subsequently loosening and unplugging aerospace connectors. The primary contribution of this paper is the ground validation of two functionalities (loosen and unplug connector) proposed in the unlocking approach. Additionally, the reasonableness of connector heating has been confirmed through experiments conducted at room temperature.

In the future, the primary objective is to integrate path planning and end-effector position feedback to achieve the functionality of re-powering the connector. To reduce the volume of a continuum robot within a maintenance satellite, a mechanism similar to a serpentine coil will be designed. Furthermore, the demanding space environment necessitates the incorporation of thermal insulation and radiation shielding layers for continuum robots.

References

[1] A. Seleem, H. El-Hussieny, and H. Ishii, "Recent Developments of Actuation Mechanisms for Continuum Robots: A Review," International Journal of Control, Automation and Systems, vol. 21, pp. 1592–1609, 2023.

[2] O. Shamilyan et al., "Intelligence and Motion Models of Continuum Robots: An Overview," in IEEE Access, vol. 11, pp. 60988-61003, 2023.

[3] Meng, D., Ouyang, X., Tan, J., Wang, X., & Liang, B. Kinematics modeling method of continuum space manipulator based on virtual discrete-jointed manipulator models. Acta Astronautica, vol. 211, pp. 257-267, 2023.

[4] S. Zhang, Q. Li, H. Yang, J. Zhao, and K. Xu, "Configuration Transition Control of a Continuum Surgical Manipulator for Improved Kinematic Performance," in IEEE Robotics and Automation Letters, vol. 4, no. 4, pp. 3750-3757, 2019.

[5] Gu, Xiaoyi, and Hongliang Ren. "A Survey of Transoral Robotic Mechanisms: Distal Dexterity, Variable Stiffness, and Triangulation." Cyborg and Bionic Systems, vol. 4, p. 0007, 2023.

[6] Wang M, Dong X, Ba W, et al. "Design, modelling and validation of a novel extra slender continuum robot for in-situ inspection and repair in aeroengine." Robotics and Computer-Integrated Manufacturing, vol. 67, 102054, 2021.

[7] Dong X, Wang M, Mohammad A, et al., "Continuum robots collaborate for safe manipulation of high-temperature flame to enable repairs in challenging environments," IEEE/ASME Transactions on Mechatronics, vol. 27, no. 5, pp. 4217-4220, 2022.

[8] Wang P, Deng B, He Z, et al. "Extensible Continuum Manipulator Toward In-situ Explosive Ordnance Disposal." Journal of Mechanisms and Robotics, vol. 15, no. 5, 051013, 2023.

[9] Gong Z, Fang X, Chen X, et al. "A soft manipulator for efficient delicate grasping in shallow water: Modeling, control, and real-world experiments." The International Journal of Robotics Research, vol. 40, no. 1, pp. 449-469, 2021.

[10] M. S. Xavier et al., "Soft Pneumatic Actuators: A Review of Design, Fabrication, Modeling, Sensing, Control and Applications," in IEEE Access, vol. 10, pp. 59442-59485, 2022.

[11] Ma B, Jiang Z, Liu Y, et al. "Advances in Space Robots for On-Orbit Servicing: A Comprehensive Review." Advanced Intelligent Systems, vol. 2023, 2200397.

[12] Zheng X, Zhu X, Chen Z, et al. "An efficient dynamic modeling and simulation method of a cable-constrained synchronous rotating mechanism for continuum space manipulator." Aerospace Science and Technology, vol. 119, 107156, 2021.

[13] Z. Mu, et al., "Dynamic feedforward control of spatial cable-driven hyper-redundant manipulators for on-orbit servicing," Robotica, vol. 37, no. 1, pp. 18-38, 2019.

[14] Peng J, Xu W, Liu T, Yuan H, Liang B. "End-effector pose and arm-shape synchronous planning methods of a hyper-redundant manipulator for spacecraft repairing." Mechanism and Machine Theory, vol. 155, 104062, 2021.

[15] Li W J, Cheng D Y, Liu X G, et al. "On-orbit service (OOS) of spacecraft: A review of engineering developments." Progress in Aerospace Sciences, vol. 108, pp. 32-120, 2019.

[16] Ge X, Zhou Q, Liu Z. "Assessment of space station on-orbit maintenance task complexity." Reliability Engineering & System Safety, vol. 193, 106661, 2020.

[17] Yan Z, Shang H, Zhao G, et al. "The Synchronization Mechanism for Solar Array with a Three-Stage Deployment." In: 44th Aerospace Mechanisms Symposium. 2018, pp. 431.

[18] SatNow. What are Solar Array Drive Mechanisms? URL: https://www.satnow.com/community/what-are-solar-array-drive-mechanisms.

[19] Ali-Akbari, Hossein Ramezani. "Design of a satellite solar panel deployment mechanism using the brushed DC motor as rotational speed damper." International Journal of Aerospace and Mechanical Engineering, vol. 12, no. 4, pp. 345-350, 2018.

[20] Lan X, Liu L, Pan C, et al. "Smart solar array consisting of shape-memory releasing mechanisms and deployable hinges." AIAA Journal, vol. 59, no. 6, pp. 2200-2213, 2021.

[21] Wilfried Stoll. BionicMotionRobot pneumatic lightweight robot with natural movement patterns. https://www.festo.com.cn/cn/zh/e/about-festo/research-and-development/bionic-learning-network/highlights-from-2015-to-2017/bionicmotionrobot-id_33307/.

[22] Jiang H, Wang Z, Jin Y, et al. "Hierarchical control of soft manipulators towards unstructured interactions." The International Journal of Robotics Research, vol. 40, no. 1, pp. 411-434, 2021.

[23] Gong Z, Fang X, Chen X, et al. "A soft manipulator for efficient delicate grasping in shallow water: Modeling, control, and real-world experiments." The International Journal of Robotics Research, vol. 40, no. 1, pp. 449-469, 2021.

[24] McMahan W, Chitrakaran V, Csencsits M, et al. "Field trials and testing of the OctArm continuum manipulator." In: Proceedings of the 2006 IEEE International Conference on Robotics and Automation, pp. 2336-2341, 2006.

[25] Dong X, Wang M, Mohammad A, et al. "Continuum robots collaborate for safe manipulation of high-temperature flame to enable repairs in challenging environments." IEEE/ASME Transactions on Mechatronics, vol. 27, no. 5, pp. 4217-4220, 2022.

[26] Yang C, Geng S, Walker I, et al. "Geometric constraint-based modeling and analysis of a novel continuum robot with shape memory alloy initiated variable stiffness." The International Journal of Robotics Research, vol. 39, no. 14, pp. 1620-1634, 2020.

[27] Zhang Yinghui, Liu Huihang, Wang Decheng. "Spring manual." China Machine Press, Beijing, 2016.

[28] Oliver-Butler K, Till J, Rucker C. "Continuum robot stiffness under external loads and prescribed tendon displacements." IEEE Transactions on Robotics, vol. 35, no. 2, pp. 403-419, 2019.

[29] Alifanov, Oleg M. et al. “Estimation of thermal properties of materials with application for inflatable spacecraft structure testing.” Inverse Problems in Science and Engineering 20 (2012): 677 - 690.

[30] Junjie Chen, Baofang Liu, “Performance evaluation of carbon nanoparticle-based thermal interface materials.” Diamond and Related Materials.